PROCEEDINGS A

rspa.royalsocietypublishing.org

Research

Cite this article: Shi Y, Luo H, Gao L, Gao C, Rogers JA, Huang Y, Zhang Y. 2015 Analyses of postbuckling in stretchable arrays of nanostructures for wide-band tunable plasmonics. *Proc. R. Soc. A* **471**: 20150632. http://dx.doi.org/10.1098/rspa.2015.0632

Received: 7 September 2015
Accepted: 1 October 2015

Subject Areas:
mechanics, mechanical engineering

Keywords:
plasmonics, analytic model, nanoscale buckling, finite-element analyses

Author for correspondence:
Yihui Zhang
e-mail: yihuizhang@tsinghua.edu.cn

Analyses of postbuckling in stretchable arrays of nanostructures for wide-band tunable plasmonics

Yan Shi[1,2,†], Hongying Luo[3,4,5,6,7,†], Li Gao[8,9,10], Cunfa Gao[2], John A. Rogers[8,9], Yonggang Huang[4,5,6,7] and Yihui Zhang[1]

[1]Center for Mechanics and Materials, AML, Department of Engineering Mechanics, Tsinghua University, Beijing 100084, People's Republic of China
[2]State Key Laboratory of Mechanics and Control of Mechanical Structures, Nanjing University of Aeronautics and Astronautics, Nanjing 210016, People's Republic of China
[3]School of Aerospace Engineering and Applied Mechanics, Tongji University, Shanghai 200092, People's Republic of China
[4]Department of Civil and Environmental Engineering, [5]Department of Mechanical Engineering, [6]Center for Engineering and Health, and [7]Skin Disease Research Center, Northwestern University, Evanston, IL 60208, USA
[8]Department of Materials Science and Engineering, Beckman Institute, and [9]Frederick Seitz Materials Research Laboratory, University of Illinois at Urbana-Champaign, Urbana, IL 61801, USA
[10]School of Electronic and Optical Engineering, Nanjing University of Science and Technology, Nanjing 210094, People's Republic of China

Plasmonic nanostructures integrated with soft, elastomeric substrates provide an unusual platform with capabilities in mechanical tuning of key optical properties, where the surface configurations can undergo large, nonlinear transformations. Arrays of planar plasmonic nanodiscs in this context can, for example, transform into three-dimensional (3D) layouts upon application of large levels of stretching to the substrate, thereby creating unique opportunities in wide-band tunable optics and photonic sensors. In this paper, a theoretical model is developed for a plasmonic system that consists of discrete nanodiscs on an elastomeric substrate,

[†]These authors contributed equally to this study.

THE ROYAL SOCIETY PUBLISHING

establishing the relation between the postbuckling configurations and the applied strain. Analytic solutions of the amplitude and wavelength during postbuckling are obtained for different buckling modes, which agree well with the results of finite-element analyses and experiment measurements. Further analyses show that increasing the nanodisc distribution yields increased 3D configurations with larger amplitudes and smaller wavelengths, given the same level of stretching. This study could serve as a design reference for future optimization of mechanically tunable plasmonic systems in similar layouts.

1. Introduction

Plasmonics is an emerging field of nanophotonics [1] in which manipulation of light at the nanoscale is possible by exploiting the properties of propagating and localized surface plasmons. Because of their novel and unique capabilities, plasmonic structures have been used in a wide range of applications, such as chiral metamaterials [2], plasmonic sensing [3], photoelectrochemistry [4], photovoltaics [5] and control of the electromagnetic field [6].

One of the key physical mechanisms in plasmonics is the excitation of localized surface plasmon resonances. As such, the plasmonic signal is quite sensitive to the surface configurations of the nanostructures as well as the surrounding dielectric environment [7]. Analytic and experimental studies [8–11] show that the surface configurations have a fundamental role in field enhancement phenomena, such as surface-enhanced Raman scattering (SERS) and metal-enhanced fluorescence (MEF) measurements [12]. Inspired by concepts of stretchable electronics [13–26] of interest in biomedical applications, stretchable plasmonics have been realized by integrating plasmonic nanostructures with elastomeric substrates, such as polydimethylsiloxane (PDMS) [27,28]. This class of plasmonic structure offers an important capability in mechanical tunability of key optical properties, through adjustment of the surface configurations. Recently, Gao *et al*. [29] realized nearly defect-free, large-scale (several square centimetres) arrays of plasmonic nanodiscs on a soft (170 kPa) elastomer material that can accommodate extremely high levels of strain (approx. 100%). Owing to the ability to tune the plasmonic resonances over an exceptionally wide range (approx. 600 nm), the resulting system has some potential for practical applications in mechanically tunable optical devices. Under large levels (e.g. greater than 50%) of stretching, nonlinear buckling processes were observed in the nanodiscs, leading to a transformation of initially planar arrays into three-dimensional (3D) configurations (figure 1*a*). Careful examination of the scanning electron microscope (SEM) images reveals that five different modes can occur and even coexist in a single, uniformly strained sample (figure 1*a*). As the 3D configurations of the nanodiscs play a critical role in the resulting plasmonic responses, quantitative control of these responses requires a clear understanding of the underlying relationship between the buckled configurations and the microstructure geometries. Previous buckling analyses [30–34]; developed for continuous ribbons/films on prestrained elastomer substrate are, however, not applicable in this plasmonic system of discrete nanodiscs.

In this paper, a systematic postbuckling analysis of plasmonic nanodiscs [29] bonded onto an elastomeric substrate was carried out, through theoretical models and finite-element analyses (FEA). The results shed light on the relation between the buckled configuration and applied tensile stretching, which is of key importance in understanding the mechanical tunability of the optical properties. The paper is outlined as follows. Section 2 takes a representative buckling mode as an example to illustrate an analytic model for determining the amplitude and wavelength in the buckled nanodiscs. In §3, this model is extended to other possible buckling modes observed in experiment. Validated by FEA and experimental results in §4, the developed model is then used to analyse the effects of nanodisc spacing and buckling modes on the wavelength and amplitude during postbuckling.

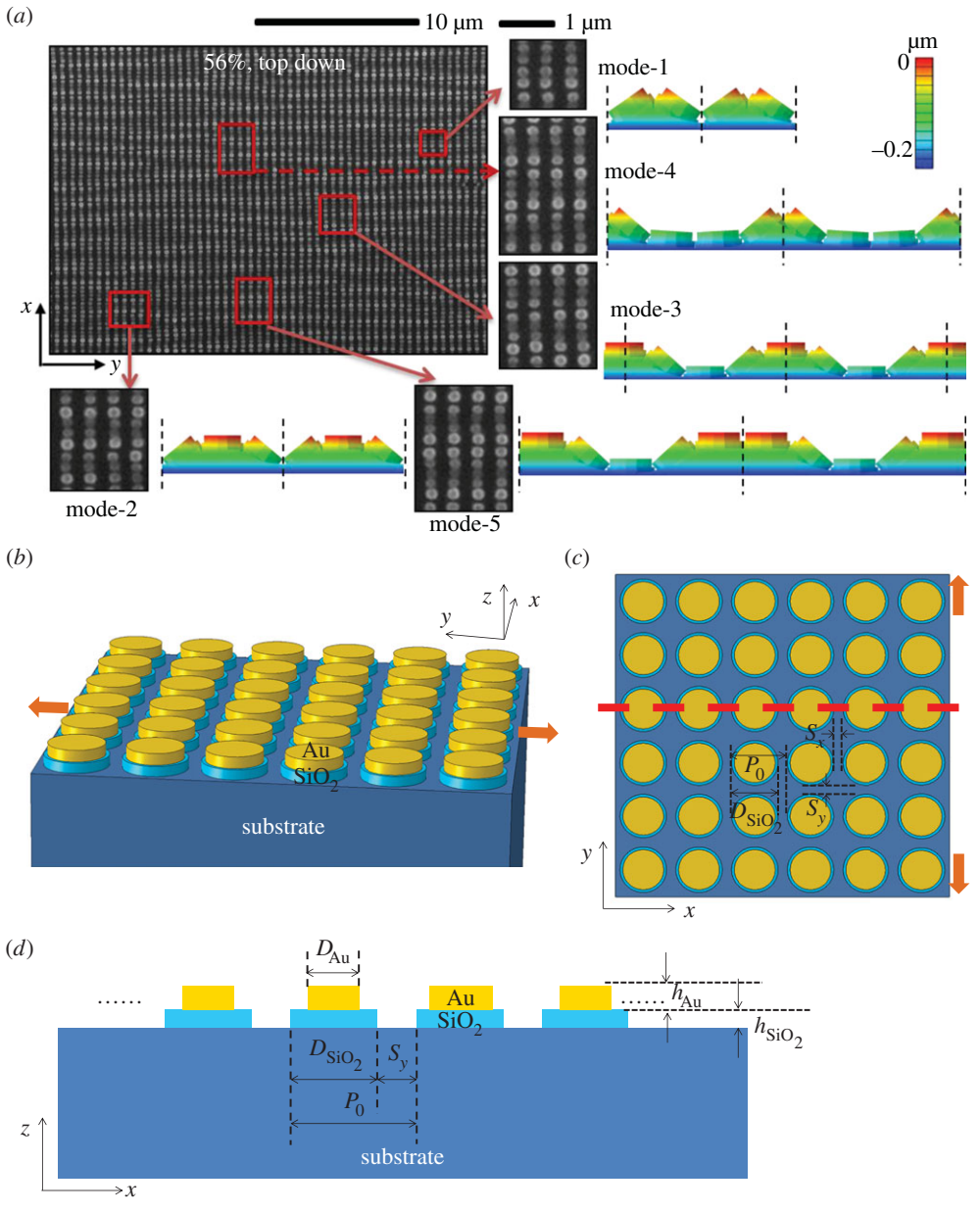

Figure 1. (*a*) Scanning electron microscope (SEM) images (top view) of the stretchable arrays of plasmonic nanodiscs that show different buckling modes across a single sample at a strain of 56%. The insets provide additional SEM images and corresponding cross-sectional views of finite-element analyses (FEA) results. Schematics of the stretchable plamonic system in the free-standing state, from different perspectives: (*b*) three-dimensional (3D) view; (*c*) top view; (*d*) a cross-sectional view that corresponds to the dashed line in figure 1c. (*a*) Adapted from Gao *et al*. [29] Copyright 2015, American Chemical Society. (Online version in colour.)

2. An analytic model of postbuckling in the plasmonic nanodiscs

Figure 1*b*, *c* presents a schematic of the stretchable plasmonic system from the 3D and top views. A square array of nanodisc bilayers consisting of gold (Au) and silicon oxide (SiO_2) was bonded onto the surface of elastomeric substrate (PDMS), in a manner that no delamination occurs, even under extreme levels (e.g. aprrox. 100%) of stretching deformation [29]. The diameters of the gold

and silicon oxide nanodiscs are D_{Au} and D_{SiO_2}, respectively, and the corresponding heights (or thicknesses) are h_{Au} and h_{SiO_2}, as shown in figure 1*d*. In the geometry of nanodiscs used in the plasmonic system, the thickness/diameter ratio (e.g. $(h_{SiO_2} + h_{Au})/D_{SiO_2}$) is typically smaller than approximately 0.4. The spacings between the adjacent nanodiscs along the *x*- and *y*-directions are represented by S_x and S_y, respectively. Without any external loading, S_x and S_y are both equal to S_0. The period (P_0) of the nanodisc array in the free-standing condition is then given by $P_0 = S_0 + D_{SiO_2}$.

A uniaxial stretching (denoted by ε_{appl}) along the *y*-axis is applied to the elastomeric substrate. At a small level of stretching, the spacing (S_y) of adjacent nanodiscs along the *y*-axis increases, while the counterpart (S_x) along the *x*-axis decreases, due to the Poisson effect. As the elastomeric substrate (with Young's modulus of $E_{substrate} = 170$ kPa) is much softer than the nanodisc (with moduli of $E_{Au} = 78$ GPa and $E_{SiO_2} = 59$ GPa for the two components), the stretching deformation is accommodated almost entirely by the substrate. This is consistent with experimental observation [29]. In this condition, the nanodiscs undergo negligible deformations, and remain almost flat. Therefore, the spacing (S_y) along the *y*-axis can be related to the applied strain by

$$S_y = P_0(1 + \varepsilon_{appl}) - D_{SiO_2}. \tag{2.1}$$

Neglecting the mechanical constraint of the nanodiscs on the overall transverse compression, the compressive strain along the transverse (i.e. *x*) direction can be written as

$$\varepsilon_{compression} = \varepsilon_x = 1 - (1 + \varepsilon_{appl})^{-1/2}, \tag{2.2}$$

where a Poisson ratio of $\nu_{substrate} = 0.5$ is used, due to the incompressibility of the substrate. As such, the spacing (S_x) along the *x*-axis is given by

$$S_x = \frac{P_0}{\sqrt{1 + \varepsilon_{appl}}} - D_{SiO_2}. \tag{2.3}$$

This transverse spacing (S_x) decreases to zero when the applied strain reaches a critical value, $\varepsilon_{appl}^{cr} = (P_0/D_{SiO_2})^2 - 1$. Additional stretching initiates a nonlinear buckling in the plasmonic structure so as to release the strain energy of the entire system, as shown in figure 1*a*. As the buckling is induced mainly by the squeezing of the stiff nanodiscs, the configuration can be well characterized by the cross section (denoted by the dashed line in figure 1*c*, and the schematic in figure 1*d*, under the un-deformed state) of the plasmonic structure.

According to the experiment results [29] in figure 1*a*, five different types of buckling modes, with the number of nanodiscs in one period ranging from two to five, can coexist in a large-area plasmonic system under a given applied strain. In the current theoretical model, the different buckling modes observed in experiment are assumed in the displacement functions, using an approach similar to that for determining the sinusoidal buckling profiles in the analyses of wrinkling in silicon ribbons bonded to pre-stretched elastomeric substrates [30,31]. In the following, the simplest buckling mode, with two nanodiscs in a representative period, is taken as an example to elucidate the analytic model. For this buckling mode (namely mode-1), two possible contact modes (type-I and type-II), illustrated in figure 2*a*,*b*, could occur, depending on the geometry of the plasmonic system and the magnitude of the applied strain. Here, the deformation of the plasmonic system is characterized mainly by the rotational angle (θ) of the nanodiscs, considering the negligible strain in the stiff nanodiscs. In this condition, the transversely compressive strain is still approximated by equation (2.2). As such, the dependence of buckling configurations on the applied strain can be determined directly through the geometric relation.

By comparing the two configurations with different contact modes, it can be noted that the type-I contact mode could occur only when the geometric parameters satisfy the following relation:

$$\Delta d_1 = L_1^2 - L_2^2 = D_{SiO_2}^2 \left[\frac{3}{4} - \frac{D_{Au}}{2D_{SiO_2}} - \left(\frac{D_{Au}}{2D_{SiO_2}} \right)^2 - 2\frac{h_{SiO_2}}{D_{SiO_2}} \frac{h_{Au}}{D_{SiO_2}} - \left(\frac{h_{Au}}{D_{SiO_2}} \right)^2 \right] > 0, \tag{2.4}$$

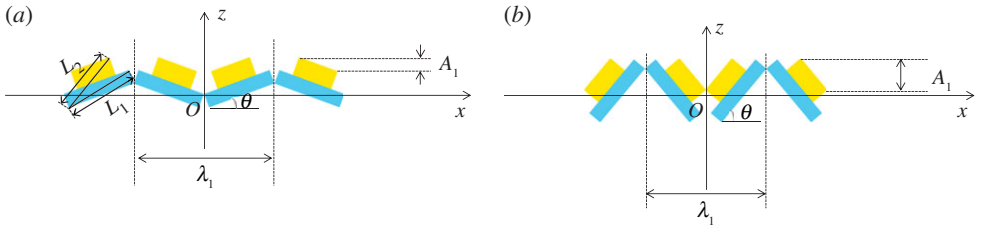

Figure 2. Schematics of two possible postbuckling configurations adopted in the analytic model, for plasmonic nanodiscs undergoing the mode-1 buckling: (*a*) with type-I contact mode: only SiO_2 nanodiscs contact each other; (*b*) with type-II contact mode: both the SiO_2 and Au nanodiscs contact the other nanodiscs. (Online version in colour.)

where L_1 and L_2 denote two characteristic lengths as illustrated in figure 2*a*, and Δd_1 is the difference of their squares. In this condition, the deformed nanodiscs undergo type-I contact mode once the buckling is triggered, and the rotational angle can be solved as

$$\theta = 2\tan^{-1}\left(\frac{\bar{h}_{SiO_2} + \sqrt{\bar{h}^2_{SiO_2} + \bar{D}^2_{SiO_2} - \varepsilon^2_{effective}}}{\bar{D}_{SiO_2} + \varepsilon_{effective}}\right), \tag{2.5}$$

where $\bar{D}_{SiO_2} = D_{SiO_2}/P_0$ and $\bar{h}_{SiO_2} = h_{SiO_2}/P_0$ correspond to the dimensionless diameter and height for the SiO_2 nanodisc, and $\varepsilon_{effective} = (1+\varepsilon_{appl})^{-1/2}$. Further increase of the applied strain will eventually move the contact points from the apices of the SiO_2 discs to the Au discs, leading to a transition of the contact mode from type-I into type-II. Based on the geometric analyses, the transition strain ($\varepsilon^{transition}_{appl}$) can be obtained as

$$\varepsilon^{transition}_{appl} = \frac{4\bar{h}^2_{Au} + (\bar{D}_{SiO_2} - \bar{D}_{Au})^2}{(2\bar{D}_{SiO_2}\bar{h}_{Au} + \bar{D}_{SiO_2}\bar{h}_{SiO_2} - \bar{D}_{Au}\bar{h}_{SiO_2})^2} - 1, \tag{2.6}$$

where $\bar{D}_{Au} = D_{Au}/P_0$ and $\bar{h}_{Au} = h_{Au}/P_0$. As the applied strain exceeds this transition strain, the deformed nanodiscs experience the type-II contact mode, with the rotational angle solved as

$$\theta = 2\tan^{-1}\left[\frac{2(\bar{h}_{SiO_2} + \bar{h}_{Au}) + \sqrt{4(\bar{h}_{SiO_2} + \bar{h}_{Au})^2 + (\bar{D}_{SiO_2} + \bar{D}_{Au})^2 - 4\varepsilon^2_{effective}}}{\bar{D}_{SiO_2} + \bar{D}_{Au} + 2\varepsilon_{effective}}\right]. \tag{2.7}$$

When $\Delta d_1 < 0$, the nanodiscs just undergo a single type of contact mode (i.e. type-II) during the postbuckling, and the type-I contact mode does not occur. In this condition, the rotational angle can be still obtained from equation (2.7).

The amplitude and wavelength are typically adopted to describe the wavy shaped configurations during postbuckling. In this study, the amplitude (A_1) is defined as the out-of-plane distance (along the z-direction) between the peak and valley of the top surfaces of all gold discs; and the wavelength (λ_1) is the projection distance of the smallest representative unit cell in the horizontal (x) direction. For the mode-1 buckling (figure 2), A_1 and λ_1 are obtained analytically as

$$A_1 = D_{Au}\sin(\theta) \quad \text{and} \quad \lambda_1 = 2P_0\varepsilon_{effective}, \tag{2.8}$$

for both the type-I and type-II contact modes. According to equations (2.4)–(2.8), the postbuckling configurations can be fully determined for different levels of applied strain.

3. Analyses of other buckling modes

In addition to the buckling mode elaborated in §2, there are four other modes that could occur in the stretchable array of nanodiscs, as shown in figure 1*a*. This section introduces analytic models to describe the postbuckling configurations for these buckling modes.

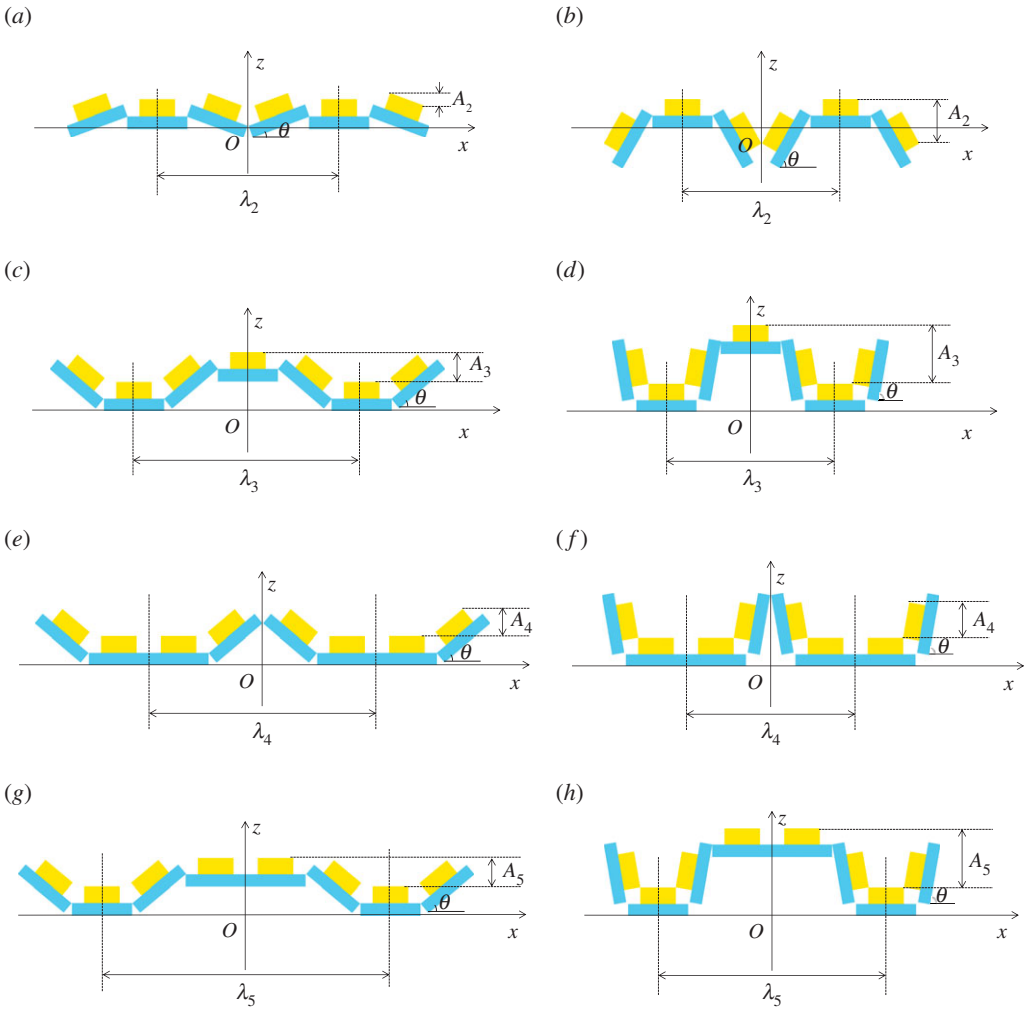

Figure 3. Schematic of the possible postbuckling configurations adopted in the analytic model, for plasmonic nanodiscs undergoing four different buckling modes: (*a*,*b*) type-I and type-II contact modes of mode-2 buckling; (*c*,*d*) type-I and type-II contact modes of mode-3 buckling; (*e*,*f*) type-I and type-II contact modes of mode-4 buckling; (*g*,*h*) type-I and type-II contact modes of mode-5 buckling. (Online version in colour.)

(a) Buckling mode with three nanodiscs in a period

Figure 3*a*,*b* presents a schematic of the buckling mode (namely mode-2) with three nanodiscs in a period. For simplicity, the contact points between the SiO_2 nanodiscs are assumed to be located at the top edges of the flat SiO_2 nanodiscs. As to be shown in the next section, this assumption provides overall reasonable predictions of postbuckling configurations. Similar to the mode-1 buckling (figure 2), two types of contact modes could also occur for this bucking mode. The type-I contact mode (figure 3*a*) occurs only when

$$\Delta d_2 = D_{SiO_2}^2 \left[\frac{3}{4} - \frac{D_{Au}}{2D_{SiO_2}} - \left(\frac{D_{Au}}{2D_{SiO_2}} \right)^2 - 2 \frac{h_{SiO_2}}{D_{SiO_2}} \frac{h_{Au}}{D_{SiO_2}} - \left(\frac{h_{Au}}{D_{SiO_2}} \right)^2 \right] > 0, \tag{3.1}$$

where Δd_2 is a parameter to judge which contact mode to appear. In the case of $\Delta d_2 > 0$, the nanodiscs undergo the type-I contact and then type-II contact, with the increase of applied strain.

The transition strain between the two different contact modes is obtained from geometric analyses as

$$\varepsilon_{\text{appl}}^{\text{transition}} = \frac{9}{[\bar{D}_{SiO_2} + (2(2\bar{D}_{SiO_2}\bar{h}_{Au} + \bar{D}_{SiO_2}\bar{h}_{SiO_2} - \bar{D}_{Au}\bar{h}_{SiO_2})/\sqrt{4\bar{h}_{Au}^2 + (\bar{D}_{SiO_2} - \bar{D}_{Au})^2})]^2} - 1. \tag{3.2}$$

Using an approach similar to the analyses of mode-1 buckling, the rotational angle (θ) of the tilted nanodiscs for mode-2 buckling can be solved as

$$\theta = 2\tan^{-1}\left[\frac{2\bar{h}_{SiO_2} + \sqrt{4\bar{h}_{SiO_2}^2 + 3(\bar{D}_{SiO_2} + 3\varepsilon_{\text{effective}})(\bar{D}_{SiO_2} - \varepsilon_{\text{effective}})}}{\bar{D}_{SiO_2} + 3\varepsilon_{\text{effective}}}\right] \quad \text{for type-I contact} \tag{3.3a}$$

and

$$\theta = 2\tan^{-1}\left[\frac{2(\bar{h}_{SiO_2} + \bar{h}_{Au}) + \sqrt{4(\bar{h}_{SiO_2} + \bar{h}_{Au})^2 + (\bar{D}_{Au} + 3\varepsilon_{\text{effective}})(2\bar{D}_{SiO_2} + \bar{D}_{Au} - 3\varepsilon_{\text{effective}})}}{\bar{D}_{Au} + 3\varepsilon_{\text{effective}}}\right]$$

for type-II contact. (3.3b)

For both contact modes, the amplitude (A_2) and wavelength (λ_2) can be written as

$$A_2 = \max\left\langle \frac{D_{Au}\sin(\theta),}{\frac{(D_{SiO_2} + D_{Au})\sin(\theta)}{2} - (h_{SiO_2} + h_{Au})\cos(\theta) + h_{Au}} \right\rangle, \tag{3.4}$$

$$\lambda_2 = 3P_0\varepsilon_{\text{effective}}. \tag{3.5}$$

(b) Buckling mode with four discs in a period

In the case of four discs in a period, two different buckling modes (namely mode-3 shown in figure 3*c*,*d*, and mode-4 shown in figure 3*e*,*f*) were observed in experiments. For both of the buckling modes, the appearance of type-I contact modes (illustrated in figure 3*c*, *e*) is determined by the same condition:

$$\Delta d_{3(4)} = D_{SiO_2}\left[1 - \frac{D_{Au}}{D_{SiO_2}} + 2\sqrt{1 + \left(\frac{h_{SiO_2}}{D_{SiO_2}}\right)^2} - 2\sqrt{\left(\frac{1}{2} + \frac{D_{Au}}{2D_{SiO_2}}\right)^2 + \left(\frac{h_{SiO_2} + h_{Au}}{D_{SiO_2}}\right)^2}\right] > 0, \tag{3.6}$$

where $\Delta d_{3(4)}$ is a parameter to judge which contact mode to appear for both the mode-3 and mode-4 buckling. In the case of $\Delta d_{3(4)} > 0$, the transition strains of these two buckling strain are the same, as given by

$$\varepsilon_{\text{appl}}^{\text{transition}} = \left[\frac{4\bar{h}_{Au}^2 + (\bar{D}_{SiO_2} - \bar{D}_{Au})^2}{2\bar{h}_{Au}(2\bar{D}_{SiO_2}\bar{h}_{Au} + \bar{D}_{SiO_2}\bar{h}_{SiO_2} - \bar{D}_{Au}\bar{h}_{SiO_2})}\right]^2 - 1. \tag{3.7}$$

The geometric analyses show that the rotational angle (θ) of the tilted nanodiscs in the two different buckling modes are also the same, i.e.

$$\theta = 2\tan^{-1}\left[\frac{\bar{h}_{SiO_2} + \sqrt{\bar{h}_{SiO_2}^2 + 4\varepsilon_{\text{effective}}(\bar{D}_{SiO_2} - \varepsilon_{\text{effective}})}}{2\varepsilon_{\text{effective}}}\right] \quad \text{for type-I contact} \tag{3.8a}$$

and

$$\theta = 2\tan^{-1}\left[\frac{\bar{h}_{SiO_2} + \bar{h}_{Au} + \sqrt{(\bar{h}_{SiO_2} + \bar{h}_{Au})^2 + 2\varepsilon_{\text{effective}}(\bar{D}_{SiO_2} + \bar{D}_{Au} - 2\varepsilon_{\text{effective}})}}{2\varepsilon_{\text{effective}}}\right]$$

for type-II contact. (3.8b)

The amplitude (A_3 and A_4) and wavelength (λ_3 and λ_4) can be written as

$$A_3 = \max\left\langle \begin{matrix}[D_{SiO_2} - h_{SiO_2}\cot(\theta)]\sin(\theta), \\ \dfrac{(D_{SiO_2} + D_{Au})\sin(\theta)}{2} - (h_{SiO_2} + h_{Au})\cos(\theta) + h_{Au}\end{matrix}\right\rangle \quad \text{for type-I contact} \tag{3.9a}$$

$$A_3 = \max\left\langle \begin{matrix} D_{Au}\sin(\theta), \\ \left[\dfrac{(D_{SiO_2} + D_{Au})}{2} - (h_{SiO_2} + h_{Au})\cot(\theta)\right]\sin(\theta) + h_{Au}\end{matrix}\right\rangle \quad \text{for type-II contact.} \tag{3.9b}$$

$$A_4 = \max\left\langle D_{Au}\sin(\theta), \frac{(D_{SiO_2} + D_{Au})\sin(\theta)}{2} - h_{Au}\right\rangle \quad \text{for type-I contact} \tag{3.10a}$$

$$A_4 = D_{Au}\sin(\theta) \quad \text{for type-II contact.} \tag{3.10b}$$

and $$\lambda_3 = \lambda_4 = 4P_0\varepsilon_{effective} \quad \text{for both type-I and type-II contacts.} \tag{3.11}$$

(c) Buckling mode with five discs in a period

Figure 3*g*,*h* shows the two different contact modes for the buckling mode (namely mode-5) with five nanodiscs in a period. The type-I contact mode (figure 3*g*) occurs only when

$$\Delta d_5 = D_{SiO_2}\left[1 - \frac{D_{Au}}{D_{SiO_2}} + 2\sqrt{1 + \left(\frac{h_{SiO_2}}{D_{SiO_2}}\right)^2} - 2\sqrt{\left(\frac{1}{2} + \frac{D_{Au}}{2D_{SiO_2}}\right)^2 + \left(\frac{h_{SiO_2} + h_{Au}}{D_{SiO_2}}\right)^2}\right] > 0, \tag{3.12}$$

where Δd_5 is a parameter to judge which contact mode to appear. For geometric parameters that yield $\Delta d_5 > 0$, the transition strain between the two different contact modes is given by

$$\varepsilon_{appl}^{transition} = \left\{\frac{5\left[4\bar{h}_{Au}^2 + (\bar{D}_{SiO_2} - \bar{D}_{Au})^2\right]}{\bar{D}_{SiO_2}(\bar{D}_{SiO_2} - \bar{D}_{Au})^2 + 4\bar{h}_{Au}(5\bar{D}_{SiO_2}\bar{h}_{Au} + 2\bar{D}_{SiO_2}\bar{h}_{SiO_2} - 2\bar{D}_{Au}\bar{h}_{SiO_2})}\right\}^2 - 1. \tag{3.13}$$

The rotational angle (θ) of the tilted nanodiscs, the amplitude (A_5) and wavelength (λ_5) of this buckling mode can be solved as

$$\theta = 2\tan^{-1}\left[\frac{2\bar{h}_{SiO_2} + \sqrt{4\bar{h}_{SiO_2}^2 - 5(\bar{D}_{SiO_2} - 5\varepsilon_{effective})(\bar{D}_{SiO_2} - \varepsilon_{effective})}}{5\varepsilon_{effective} - \bar{D}_{SiO_2}}\right] \quad \text{for type-I contact} \tag{3.14a}$$

and $$\theta = 2\tan^{-1}\left[\frac{2(\bar{h}_{SiO_2} + \bar{h}_{Au}) + \sqrt{4(\bar{h}_{SiO_2} + \bar{h}_{Au})^2 - (\bar{D}_{SiO_2} - 5\varepsilon_{effective})(3\bar{D}_{SiO_2} + 2\bar{D}_{Au} - 5\varepsilon_{effective})}}{5\varepsilon_{effective} - \bar{D}_{SiO_2}}\right]$$

for type-II contact. (3.14b)

$$A_5 = \max\left\langle \begin{matrix}[D_{SiO_2} - h_{SiO_2}\cot(\theta)]\sin(\theta), \\ \dfrac{(D_{SiO_2} + D_{Au})\sin(\theta)}{2} - h_{Au}\end{matrix}\right\rangle \quad \text{for type-I contact} \tag{3.15a}$$

and $$A_5 = \max\left\langle \begin{matrix} D_{Au}\sin(\theta), \\ \left[\dfrac{(D_{SiO_2} + D_{Au})}{2} - (h_{SiO_2} + h_{Au})\cot(\theta)\right]\sin(\theta) + h_{Au}\end{matrix}\right\rangle \quad \text{for type-II contact.} \tag{3.15b}$$

$$\lambda_5 = 5P_0\varepsilon_{effective} \quad \text{for both the type-I and type-II contacts.} \tag{3.16}$$

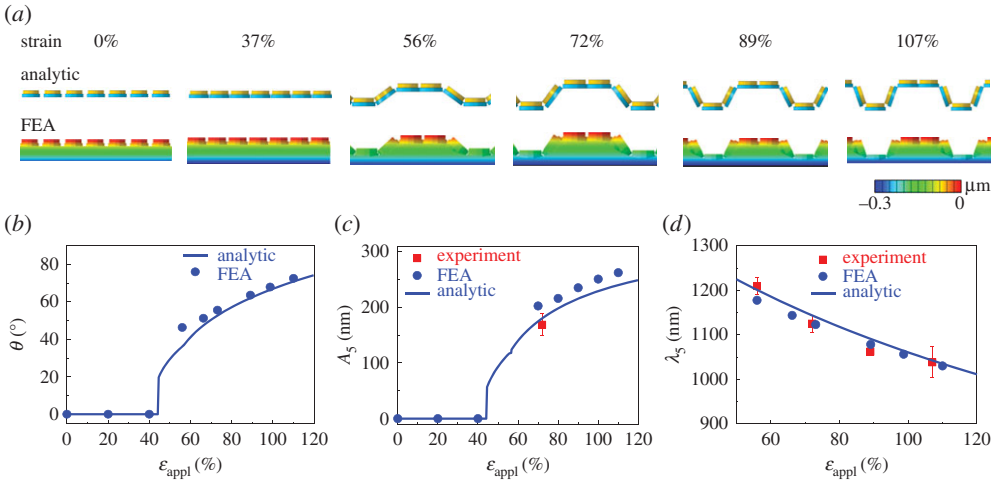

Figure 4. (*a*) Cross-sectional view of the plasmonic nanodiscs (with mode-5 buckling) predicted by analytic and FEA models, respectively. The colour represents the out-of-plane coordinate. (*b*) Rotational angle of tilted nanodiscs, (*c*) amplitude and (*d*) wavelength during the postbuckling versus the applied strain, based on analytic model, FEA and experiment. (Online version in colour.)

4. Effects of bucking mode and nanodisc spacing on the wavelength and amplitude

Full three-dimensional FEA is carried out to validate the above analytic model. In the FEA, a uniaxial stretching is applied to the elastomeric substrate (PDMS), where the rigid bi-layer nanodiscs are mounted on its top surface. The interfaces between the nanodiscs and the substrate are assumed to be sufficiently strong, such that no delamination occurs. For the plasmonic nanodiscs adopted in the experiment of Gao *et al*. [29], the geometric parameters are given by $P_0 = 300$nm, $D_{SiO_2} = 250$ nm, $D_{Au} = 220$nm, $h_{SiO_2} = 40$nm and $h_{Au} = 45$ nm. The elastic properties (Young's modulus E and Poisson's ratio ν) of the various components are $E_{substrate} = 170$ kPa and $\nu_{substrate} = 0.49$ for substrate; $E_{Au} = 78$ GPa and $\nu_{Au} = 0.44$ for gold; and $E_{SiO_2} = 59$ GPa and $\nu_{SiO_2} = 0.24$ for silicon oxide. Eight-node 3D solid elements in ABAQUS Standard [35] are used for both the nanodiscs and the substrate, with refined meshes to ensure computational accuracy. In the postbuckling analyses, the various buckling modes (figure 1*a*) observed in the experiments are implemented as initial imperfections through force loading. These artificial forces are removed when the nanodiscs come into contact. Periodical boundary conditions are adopted along two in-plane principal directions (i.e. x- and y-axes in figure 1*b*) to reduce the computational cost, and the number of nanodiscs required in the simulations depends on the specific buckling mode investigated. Through the above FEA, the evolution of postbuckling configurations for each buckling mode can be determined for different levels of applied strain.

Figure 4*a* presents analytic predictions and FEA calculations of the stretching-induced geometry change in the plasmonic nanodisc system with the mode-5 buckling. Good accordance between the analytic and FEA results can be found in the entire range of strain (from 0 to 107%). The rotational angle of the tilted nanodiscs is plotted as a function of the applied strain in figure 4*b*, which increases with increasing applied strain, reaching approximately 72° at 107% strain. The nonlinear dependences of amplitude and wavelength based on the analytic model are shown in figure 4*c*,*d*, which agree well with both the FEA calculations and the experimental measurements [29]. These variations of amplitude and wavelength in the current discrete system of nanodiscs are in qualitative consistence with that in continuous hard films bonded onto prestrained elastomeric

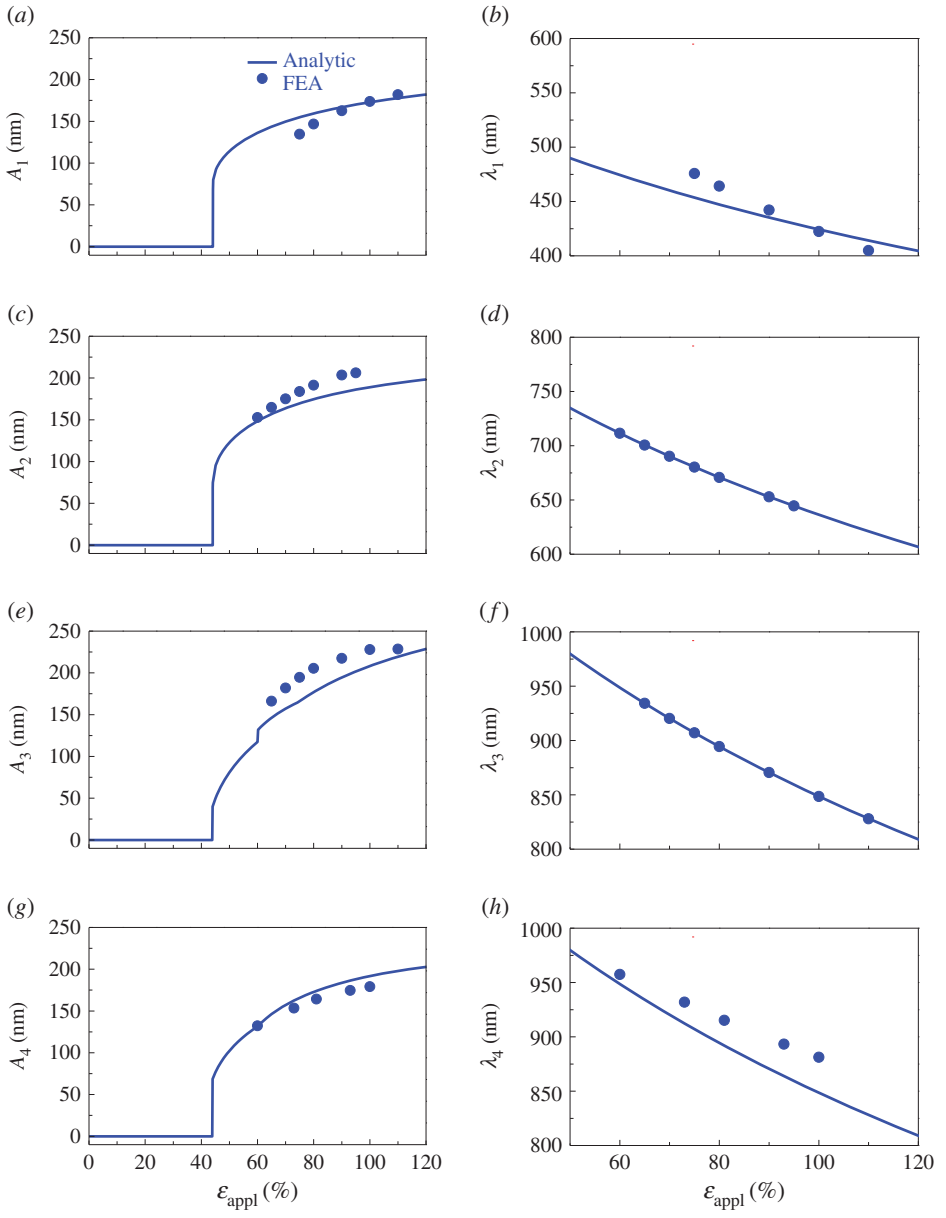

Figure 5. Analytic prediction and FEA calculations of the amplitude and wavelength during postbuckling with different modes: (*a*,*b*) for mode-1; (*c*,*d*) for mode-2; (*e*,*f*) for mode-3; and (*g*,*h*) for mode-4. (Online version in colour.)

substrate [31], although their magnitudes are much smaller (e.g. by an order of magnitude), given the same material system and the same thickness of hard material. For the other buckling modes (mode-1 to mode-4), the amplitude also increases and the wavelength decreases with the increase of applied strain, as shown in figure 5. Here, the analytic results agree reasonably well with FEA results for all of the buckling modes.

After validating the developed analytic model, we then use this model to analyse the effect of an important design parameter, i.e. the spacing/period ratio (S_0/P_0) that decides the areal coverage of the plasmonic nanodiscs. The stretchable plasmonic systems with the same material composition and nanodisc geometry as that in Gao *et al*. [29] are investigated, while the spacing

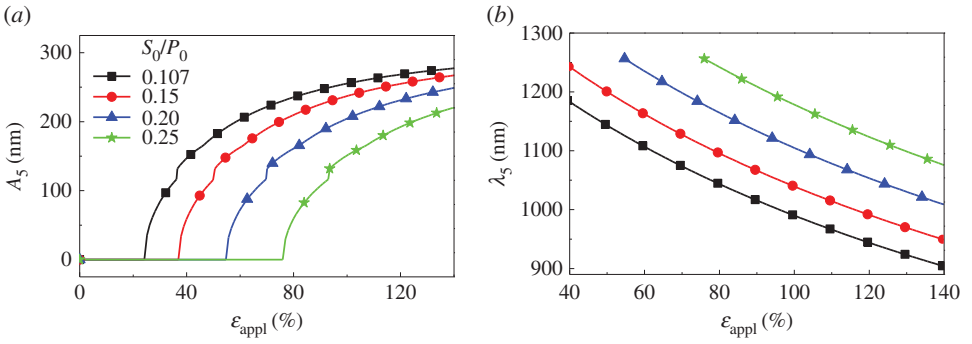

Figure 6. Analytic prediction of (*a*) amplitude and (*b*) wavelength during the postbuckling (with mode-5) versus the applied strain, for four different spacing/period ratios (S_0/P_0). (Online version in colour.)

(S_0) is varied, resulting in different spacing/period ratios ranging from approximately 0.11 to 0.25. A representative buckling mode (i.e. mode-5) is taken as an example to show this effect on the amplitude and wavelength, as shown in figure 6. The plasmonic system with a denser nanodisc distribution (corresponding to a smaller S_0/P_0) provides larger amplitude and smaller wavelength during postbuckling under the same strain. This indicates a wider range of buckling amplitude that can be tuned by the same level of mechanical stretching, for the system with a smaller S_0/P_0.

5. Concluding remarks

This paper presents a theoretical study of postbuckling in stretchable arrays of discrete plasmonic nanodiscs, through combined analytic modelling and FEA. Two different contact modes of the nanodiscs are taken into account, and their transition is explored. Analytic solution of the postbuckling configurations, in terms of the wavelength and amplitude are obtained for different types of buckling modes, which agree reasonably well with FEA and experimental results. Further calculations on the effect of spacing/period ratio show that a denser nanodisc distribution yields more evident 3D nanodisc configurations (with larger amplitudes and smaller wavelengths) during postbuckling. The analytic model developed is useful for future design and optimization of mechanically tunable plasmonic structures.

Data accessibility. Experimental data are available from Gao *et al*. [29] (doi:10.1021/acsnano.5b00716).

Authors' contributions. Y.S. carried out the analytic modelling, analysed the data and drafted the manuscript; H.L. carried out the FEA and participated in data analysis and discussions; L.G. participated in data analysis and discussions; C.G. participated in the analytic modelling and discussions; J.A.R. and Y.H. analysed the data and revised the manuscript; Y.Z. designed the study, analysed the data and finalized the manuscript. All authors gave final approval for publication.

Competing interests. We declare we have no competing interests.

Funding. Y.Z. acknowledges support from the Thousand Young Talents Program of China, the National Science Foundation of China (grant no. 11502129) and the National Basic Research Program of China (grant no. 2015CB351900). Y.H. and J.A.R. acknowledge the support from NSF (CMMI-1300846 and CMMI-1400169) and the NIH (grant no. R01EB019337).

Acknowledgements. We thank Dr Yewang Su (from Chinese Academy of Sciences) for helpful discussions on the analytic modelling.

References

1. Lal S, Link S, Halas NJ. 2007 Nano-optics from sensing to waveguiding. *Nat. Photonics* **1**, 641–648. (doi:10.1038/nphoton.2007.223)

2. Gansel JK, Thiel M, Rill MS, Decker M, Bade K, Saile V, von Freymann G, Linden S, Wegener M. 2009 Gold helix photonic metamaterial as broadband circular polarizer. *Science* **325**, 1513–1515. (doi:10.1126/science.1177031)
3. McPhillips J, McClatchey C, Kelly T, Murphy A, Jonsson MP, Wurtz GA, Winfield RJ, Pollard RJ. 2011 Plasmonic sensing using nanodome arrays fabricated by soft nanoimprint lithography. *J. Phys. Chem. C*. **115**, 15 234–15 239. (doi:10.1021/jp203216k)
4. Thomann I, Pinaud BA, Chen Z, Clemens BM, Jaramillo TF, Brongersma ML. 2011 Plasmon enhanced solar-to-fuel energy conversion. *Nano Lett*. **11**, 3440–3446. (doi:10.1021/nl201908s)
5. Atwater HA, Polman A. 2010 Plasmonics for improved photovoltaic devices. *Nat. Mater*. **9**, 205–213. (doi:10.1038/nmat2629)
6. Novothy L, Hecht B. 2006 *Principles of nano-optics*. Cambridge, UK: Cambridage University Press.
7. Kumar GVP. 2012 Plasmonic nano-architectures for surface enhanced Raman scattering: a review. *J. Nanophotonics* **6**, 064503. (doi:10.1117/1.jnp.6.064503)
8. Truegler A, Tinguely J-C, Krenn JR, Hohenau A, Hohenester U. 2011 Influence of surface roughness on the optical properties of plasmonic nanoparticles. *Phys. Rev. B* **83,** 081412. (doi:10.1103/PhysRevB.83.081412)
9. Hoffmann A, Lenkefi Z, Szentirmay Z. 1998 Effect of roughness on surface plasmon scattering in gold films. *J. Phys-Condens. Mat*. **10**, 5503–5513. (doi:10.1088/0953-8984/10/24/025)
10. Rodriguez-Fernandez J, Funston AM, Perez-Juste J, Alvarez-Puebla RA, Liz-Marzan LM, Mulvaney P. 2009 The effect of surface roughness on the plasmonic response of individual sub-micron gold spheres. *Phys. Chem. Chem. Phys*. **11**, 5909–5914. (doi:10.1039/b905200n)
11. Peng H-I, Strohsahl CM, Leach KE, Krauss TD, Miller BL. 2009 Label-free DNA detection on nanostructured Ag surfaces. *Acs Nano* **3**, 2265–2273. (doi:10.1021/nn900112e)
12. D'Agostino S, Della Sala F. 2011 Silver nanourchins in plasmonics: theoretical investigation on the optical properties of the branches. *J. Phys. Chem. C* **115**, 11 934–11 940. (doi:10.1021/jp202229y)
13. Khang DY, Jiang HQ, Huang Y, Rogers JA. 2006 A stretchable form of single-crystal silicon for high-performance electronics on rubber substrates. *Science* **311**, 208–212. (doi:10.1126/science.1121401)
14. Kim D-H *et al* 2008 Stretchable and foldable silicon integrated circuits. *Science* **320**, 507–511. (doi:10.1126/science.1154367)
15. Xiao J, Carlson A, Liu ZJ, Huang Y, Jiang H, Rogers JA. 2008 Stretchable and compressible thin films of stiff materials on compliant wavy substrates. *Appl. Phys. Lett*. **93**, 013109. (doi:10.1063/1.2955829)
16. Rogers JA, Someya T, Huang Y. 2010 Materials and mechanics for stretchable electronics. *Science* **327**, 1603–1607. (doi:10.1126/science.1182383)
17. Zhu Y, Xu F. 2012 Buckling of aligned carbon nanotubes as stretchable conductors: a new manufacturing strategy. *Adv. Mater*. **24**, 1073–1077. (doi:10.1002/adma.201103382)
18. Zhang Y, Xu S, Fu H, Lee J, Su J, Hwang K-C, Rogers JA, Huang Y. 2013 Buckling in serpentine microstructures and applications in elastomer-supported ultra-stretchable electronics with high areal coverage. *Soft Matter* **9**, 8062–8070. (doi:10.1039/c3sm51360b)
19. Huang Y, Wang Y, Xiao L, Liu H, Dong W, Yin Z. 2014 Microfluidic serpentine antennas with designed mechanical tunability. *Lab Chip* **14**, 4205–4212. (doi:10.1039/c4lc00762j)
20. Widlund T, Yang S, Hsu Y-Y, Lu N. 2014 Stretchability and compliance of freestanding serpentine-shaped ribbons. *Int. J. Solids Struct*. **51**, 4026–4037. (doi:10.1016/j.ijsolstr.2014.07.025)
21. Song Z *et al*. 2014 Origami lithium-ion batteries. *Nat. Commun*. **5**, 3140. (doi:10.1038/ncomms4140)
22. Zhang Y, Fu H, Xu S, Fan JA, Hwang K-C, Jiang J, Rogers JA, Huang Y. 2014 A hierarchical computational model for stretchable interconnects with fractal-inspired designs. *J. Mech. Phys. Solids* **72**, 115–130. (doi:10.1016/j.jmps.2014.07.011)
23. Jang K-I *et al*. 2015 Soft network composite materials with deterministic and bio-inspired designs. *Nat. Commun*. **6**, 6566. (doi:10.1038/ncomms7566)
24. Lu N, Yang S. 2015 Mechanics for stretchable sensors. *Curr. Opin. Solid State Mater*. Sci. **19**, 149–159. (doi:10.1016/j.cossms.2014.12.007)
25. Yao S, Zhu Y. 2015 Nanomaterial-enabled stretchable conductors: strategies, materials and devices. *Adv. Mater*. **27**, 1480–1511. (doi:10.1002/adma.201404446)

26. Song J. 2015 Mechanics of stretchable electronics. *Curr. Opin. Solid State Mater. Sci.* **19**, 160–170. (doi:10.1016/j.cossms.2015.01.004)
27. Pryce IM, Aydin K, Kelaita YA, Briggs RM, Atwater HA. 2010 Highly strained compliant optical metamaterials with large frequency tunability. *Nano Lett.* **10**, 4222–4227. (doi:10.1021/nl102684x)
28. Aksu S, Huang M, Artar A, Yanik AA, Selvarasah S, Dokmeci MR, Altug H. 2011 Flexible plasmonics on unconventional and nonplanar substrates. *Adv. Mater.* **23**, 4422–4430. (doi:10.1002/adma.201102430)
29. Gao L *et al.* 2015 Optics and nonlinear buckling mechanics in large-area, highly stretchable arrays of plasmonic nano structures. *ACS Nano* **9**, 5968–5975. (doi:10.1021/acsnano.5b00716)
30. Huang ZY, Hong W, Suo Z. 2005 Nonlinear analyses of wrinkles in a film bonded to a compliant substrate. *J. Mech. Phys. Solids* **53**, 2101–2118. (doi:10.1016/j.jmps.2005.03.007)
31. Jiang H, Khang D-Y, Song J, Sun Y, Huang Y, Rogers JA. 2007 Finite deformation mechanics in buckled thin films on compliant supports. *Proc. Natl Acad. Sci. USA* **104**, 15 607–15 612. (doi:10.1073/pnas.0702927104)
32. Song J, Jiang H, Liu ZJ, Khang DY, Huang Y, Rogers JA, Lu C, Koh CG. 2008 Buckling of a stiff thin film on a compliant substrate in large deformation. *Int. J. Solids Struct.* **45**, 3107–3121. (doi:10.1016/j.ijsolstr.2008.01.023)
33. Zhang Y *et al.* 2014 Experimental and theoretical studies of serpentine microstructures bonded to prestrained elastomers for stretchable electronics. *Adv. Funct. Mater.* **24**, 2028–2037. (doi:10.1002/adfm.201302957)
34. Wang Q, Zhao X. 2014 Phase diagrams of instabilities in compressed film-substrate systems. *J. Appl. Mech.* **81**, 051004. (doi:10.1115/1.4025828)
35. ABAQUS Analysis User's ManualV6.9. 2009 Pawtucket, RI: Dassault Systèmes.